

# AIRS deconvolution and the translation of AIRS to CrIS radiances with applications for the IR climate record

\*\*\*\* DRAFT \*\*\*\*

Howard E. Motteler  
L. Larrabee Strow

UMBC Atmospheric Spectroscopy Lab  
Joint Center for Earth Systems Technology

October 17, 2017

## 1 Introduction

Upwelling infrared radiation as measured by the AIRS [1] and CrIS [2, 10] sounders is a significant part of the long term climate record. AIRS and CrIS have similar sampling patterns [7]. We often want to compare radiances, and would like to treat this as a single data set for the analysis of long term trends. However the instruments have different spectral resolutions, channel response functions, and band spans. As a step in addressing this problem we consider the translation of channel radiances from AIRS to standard resolution CrIS.

In addition to our AIRS to CrIS translation we make regular use of an IASI to CrIS translation for evaluating simultaneous nadir overpasses (SNOs) [3], and have implemented and tested IASI to AIRS and CrIS to AIRS translations as well. The translations from IASI includes deapodization (a form of deconvolution) before reconvolution to the translation target, and work very well. Ranking these translations by accuracy in comparison with calculated reference truth, we have IASI to CrIS, IASI to AIRS, AIRS to CrIS, and finally CrIS to AIRS [6]. But aside from AIRS to CrIS the methods used are for the most part

conventional.

Our translation from AIRS to CrIS has some novel features. AIRS is a grating spectrometer with a distinct response function for each channel determined by the focal plane geometry, while CrIS is a Michelson interferometer with a sinc response function after calibration and corrections. In section 2 we show how to take advantage of our detailed knowledge of the AIRS spectral response functions (SRFs) and their overlap to deconvolve channel radiances to a resolution-enhanced intermediate representation, typically a  $0.1 \text{ cm}^{-1}$  grid, the approximate resolution of the tabulated AIRS SRFs. This intermediate representation can then be reconvolved to an alternate instrument specification. Section 3 gives details and validation tests for the AIRS to CrIS translation and section 4 for translation to an idealized grating model. For both cases deconvolution followed by reconvolution is shown to work significantly better than conventional interpolation. Both methods can be further improved with a statistical correction. In section 5 we consider a purely statistical approach to such translations, and compare these with deconvolution.

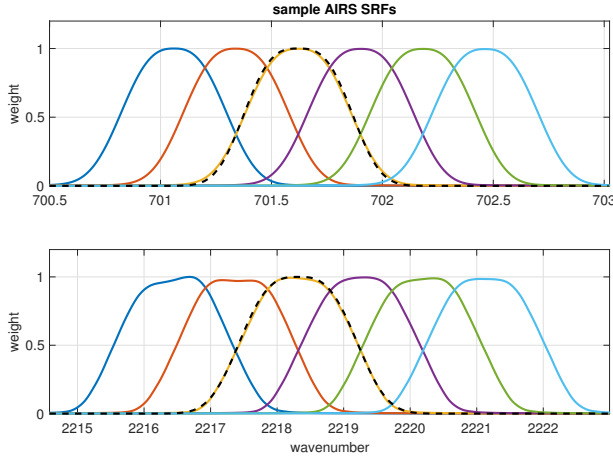


Figure 1: sample AIRS spectral response functions from the low and high ends of the band. The dashed line is a generalized Gaussian function.

## 2 AIRS Deconvolution

The AIRS spectral response functions model channel response as a function of frequency and associate channels with nominal center frequencies. Each AIRS channel  $i$  has an associated spectral response function or SRF  $\sigma_i(v)$  such that the channel radiance  $c_i = \int \sigma_i(v)r(v) dv$ , where  $r$  is radiance at frequency  $v$ . The center or peak of  $\sigma_i$  is the nominal channel frequency.

Figure 1 shows typical AIRS SRFs from the low and high ends of the band. Note the significant overlap in the wings. This can allow for a deconvolution to recover resolution beyond that of the response functions considered individually. The SRFs are not necessarily symmetrical, especially at the high end of the band. The dashed line on top of the third SRF in each group is a fit for a generalized Gaussian, which we consider in more detail later in this section. Figure 2 shows channel spacing and resolving power for the AIRS L1c channel set [4]. The variable channel spacing and resolving power are due to the modular structure of the focal plane. Although not entirely regular—that is, not a simple function of frequency—the L1c channel set is more regular than the L1b channel set from which it is derived, and we mainly consider the L1c

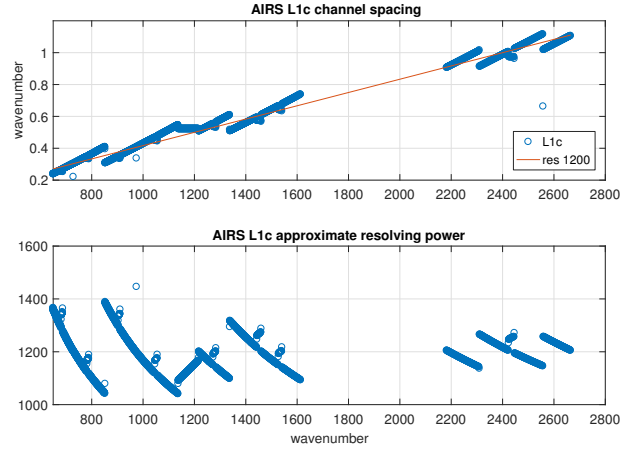


Figure 2: AIRS L1c channel spacing and derived resolving power.

set here.

Suppose we have  $n$  channels and a frequency grid  $\vec{v}$  of  $k$  points spanning the union of the domains of the functions  $\sigma_i$ . The grid step size for our applications is often  $0.0025 \text{ cm}^{-1}$ , the default resolution for upwelling radiances calculated with kcarta [11]. Let  $S_k$  be an  $n \times k$  array such that  $s_{i,j} = \sigma_i(v_j)/w_i$ , where  $w_i = \sum_j \sigma_i(v_j)$ , that is where row  $i$  is  $\sigma_i(v)$  tabulated at the grid  $\vec{v}$  and normalized so the row sum is 1. If the channel centers are in increasing order  $S_k$  is banded, and if they are not too close (as is the case for a few of the L1b channels) the rows are linearly independent.  $S_k$  is a linear transform whose domain is radiance at the grid  $\vec{v}$  and whose range is channel radiances. If  $r$  is radiance at the grid  $\vec{v}$ , then  $c = S_k r$  gives a good approximation of the channel radiances  $c_i = \int \sigma_i(v)r(v) dv$ . In practice this is how we convolve kcarta or other high resolution calculated radiances to get AIRS channel radiances, for example for reference truth or “true AIRS” for the tests shown here.

For the AIRS to CrIS and other translations we are mainly interested in the transform  $S_b$  for SRFs at an intermediate resolution, typically  $0.1 \text{ cm}^{-1}$ . This is the approximate resolution of the SRF measurements and convenient for reconvolution to the CrIS user grid. So let  $\vec{v}_b = v_1, v_2, \dots, v_m$  be a  $0.1 \text{ cm}^{-1}$

grid spanning the domains of the functions  $\sigma_i$ . Similar to  $S_k$ , let  $S_b$  be an  $n \times m$  array where row  $i$  is  $\sigma_i(v)$  tabulated at the  $\vec{v}_b$  grid, with rows normalized to 1. If  $r$  is radiance at the  $\vec{v}_b$  grid, then  $c = S_b r$  is still a reasonable approximation of  $\int \sigma_i(v) r(v) dv$ .

For our application we want to start with  $c$  and find  $r$ , that is to deconvolve  $c$  by solving  $S_b r = c$  for  $r$ . Since  $m < k$  the system is underdetermined. We take the Moore-Penrose pseudoinverse [13] of  $S_b$  to get  $r_0 = S_b^{-1} c$ . This gives a minimal solution, in the sense that  $\|r_0\|_2 \leq \|r_j\|_2$  for all  $r_j$  satisfying  $S_b r_j = c$ . The condition number for  $S_b$  as built from the L1c channels is  $\|S_b\|_2 \|S_b^{-1}\|_2 = 115$ , which is tolerable.

Although our main goal is to reconvolve the  $0.1 \text{ cm}^{-1}$  intermediate representation to the CrIS or other user grids, we first compare the deconvolved radiances with reference truth from a direct convolution to the intermediate grid. The choice of response functions for the direct convolution is not obvious, since the deconvolution is undoing—at least to some extent—the effects of the AIRS SRF convolutions. We chose a generalized Gaussian [12] of the form

$$w(v, v_0, \text{FWHM}) = \exp \left( - \left( \frac{(v - v_0)^2}{2c^2} \right)^{1.5} \right)$$

where  $c = \text{FWHM}/(2\sqrt{2\ln 2})$  and  $v_0$  is the desired channel center. The exponent 1.5 was chosen to give an approximate match to AIRS SRFs with the same FWHM and channel centers, though without the fine structure and variation of the measured SRFs. Figure 1 shows two such generalized Gaussians paired with the corresponding AIRS SRFs. We used the same functions as reference truth for the  $0.1 \text{ cm}^{-1}$  intermediate grid with  $\text{FWHM} = v_i/2000$ , where  $v_i$  are the grid frequencies. This represents a hypothetical grating spectrometer with a resolving power of 2000, oversampled to the  $0.1 \text{ cm}^{-1}$  grid. The residual was roughly minimized for a resolving power of 2000, as shown here. We also tried the generalized Gaussian with a fixed FWHM for values 0.4, 0.6, and 0.8, and a sinc basis with a spacing of  $0.2 \text{ cm}^{-1}$ , all of which gave larger residuals.

The AIRS deconvolution gives a modest resolution

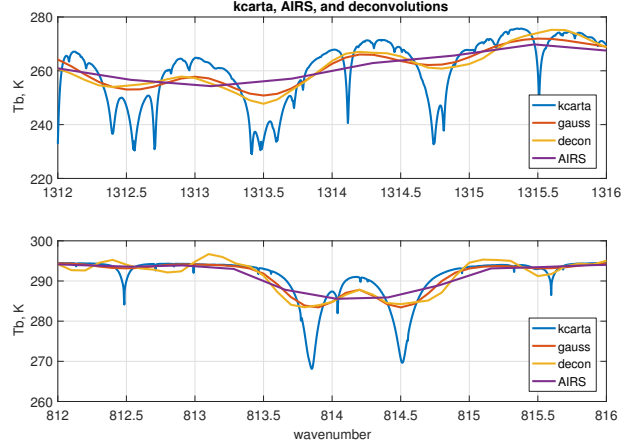


Figure 3: details from fitting profile 1 for kcarta, direct convolution to the  $0.1 \text{ cm}^{-1}$  grid (“gauss”), deconvolved AIRS, and true AIRS.

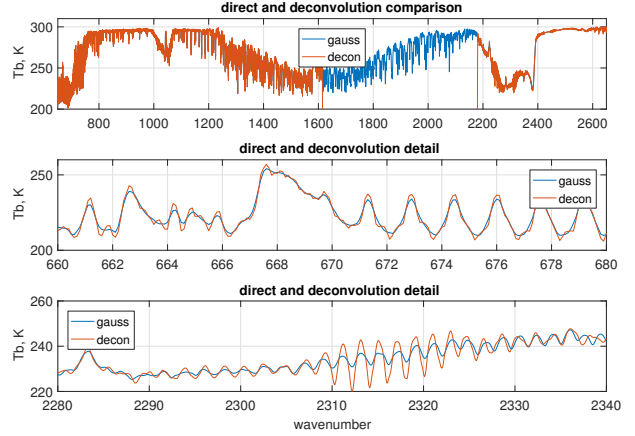


Figure 4: spectra from fitting profile 1 for direct convolution to the  $0.1 \text{ cm}^{-1}$  grid (“gauss”) and deconvolved AIRS

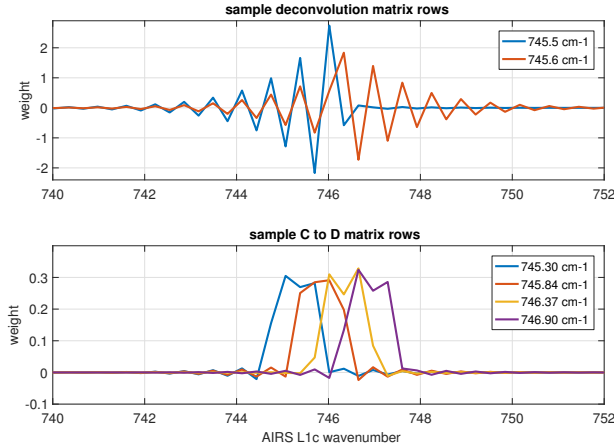


Figure 5: sample adjacent rows for the deconvolution and L1c to L1d transforms

enhancement, at the cost of added artifacts and noise. Figure 3 shows details of kcarta, direct convolution to the  $0.1 \text{ cm}^{-1}$  grid (“gauss”), deconvolution, and AIRS spectra for fitting profile 1 [8, 9]. In the first subplot we see the deconvolution is capturing some of the fine structure in the kcarta data that is present in the direct convolution but not in the AIRS data. In the second subplot we see the deconvolution (and direct convolution) resolving a pair of close lines that are not resolved at the AIRS L1c resolution. But we also see some ringing that is not present in the direct convolution. Figure 4 shows the full spectra from fitting profile 1, along with sample details from the low and high ends of the band, for the deconvolution and direct convolution to the intermediate grid. In the details we see some overshoot and ringing in the deconvolution. But as noted we do not propose using the deconvolved radiances directly, they are an intermediate step in reconvolution to a lower resolution.

Figure 5 shows a pair of typical adjacent rows of the deconvolution matrix  $S_b^{-1}$  in the first subplot. Row  $i$  of  $S_b^{-1}$  is the weights applied to L1c channel radiances to synthesize the deconvolved radiance  $r_i$  at the intermediate grid frequency  $v_i$ . The oscillation shows we are taking the closest AIRS channel, subtracting weighted values for channels  $\pm 1$  step away, adding weighted values for channels  $\pm 2$  steps away, and so

on, with the weights decreasing quickly as we move away from  $v_i$ , with eight to ten L1c channels making a significant contribution to each deconvolution grid point.

The second subplot shows four adjacent rows of the matrix  $S_d \cdot S_b^{-1}$ , which takes L1c to L1d channel radiances. (The L1d radiances are discussed in a later section; here they are of interest mainly as a typical reconvolution.) Both matrices are banded but the bands are narrower in the second, with three to five L1c channels contributing significantly to each L1d channel. The range of influence is significant since for example we may want to see which L1d channels are derived in part from the subset of synthetic L1c channels.

### 3 AIRS to CrIS translation

Given AIRS deconvolution to a  $0.1 \text{ cm}^{-1}$  intermediate grid, reconvolution to the CrIS user grid is straightforward. For the CrIS standard resolution mode the channel spacing is  $0.625 \text{ cm}^{-1}$  for the LW,  $1.25 \text{ cm}^{-1}$  for the MW, and  $2.5 \text{ cm}^{-1}$  for the SW bands. For each CrIS band, we (1) find the AIRS and CrIS band intersection, (2) apply a bandpass filter to the deconvolved AIRS radiances restricting them to the intersection, with a rolloff outside the intersection, and (3) reconvolve the filtered spectra to the CrIS user grid with a zero-filled double Fourier transform [5].

Translations are tested by comparison with calculated reference truth. We start with a set of atmospheric profiles and calculate upwelling radiance at a  $0.0025 \text{ cm}^{-1}$  grid with kcarta [11] over a band spanning the domains of the AIRS and CrIS response functions. “True AIRS” is calculated by convolving the kcarta radiances with AIRS SRFs and “true CrIS” by convolving kcarta radiances to a sinc basis at the CrIS user-grid. True AIRS is then translated to CrIS to get “AIRS CrIS”, and this is compared with true CrIS. Figure 6 shows sample spectra for true AIRS, deconvolved AIRS, true CrIS and AIRS CrIS. The difference between true CrIS and AIRS CrIS is hard to see at this level of detail, and for the remainder of this paper we will mainly show explicit differences.

For most tests we use a set of 49 fitting profiles

spanning a wide range of clear atmospheric conditions, initially chosen for testing radiative transfer codes [8, 9]. The set is largely uncorrelated; reducing the reconstruction residual to 0.02 K requires 48 left-singular vectors. (Details of this correlation measure are given in an appendix.) For statistical correction and the direct regression discussed in section 5 we also use a set of 7377 radiances calculated from all-sky (clear and cloudy) AIRS profiles spanning several consecutive days as the dependent set. This set is moderately correlated; reducing the reconstruction residual to 0.02 K requires 260 left-singular vectors. Splitting the 7377 profile set into dependent and independent subsets and comparing residuals from the independent subset with residuals from the 49-profile set, we found residuals from the latter are consistently larger, suggesting it makes for a stricter test. So for the results shown here the test or independent set is always the 49-profile set, while for tests requiring fitting the 7377 profile is used as the dependent set.

Figures 7, 8, and 9 show the mean and standard deviation of true CrIS minus AIRS CrIS for the 49 fitting profiles, with and without Hamming apodization, for each of the CrIS bands. Figure 10 summarizes these results for Hamming apodized radiances. The residual has a high frequency component with a period of 2 channel steps that is significantly reduced by the apodization. The constant or DC bias is very close to zero for the apodized residuals.

Some regularity remains in the apodized residual, including the oscillation with a period of two channel steps. Up to this point there has been no statistical component to our translation, beyond the choice of test set for validation. We feel it is important to be clear about any steps that require statistical fitting. That said, a simple linear correction can give a significantly further reduction of the residuals. For such tests as noted we use the set of 7377 mostly cloudy AIRS profiles as the dependent set and the 49 profile set the independent or test set.

We compare three such corrections. These are done with a separate regression for each CrIS channel, and so introduce no cross-correlations. Let  $t_i^{TC}$  be true CrIS and  $t_i^{AC}$  AIRS to CrIS brightness temperatures for CrIS channel  $i$ , from the dependent

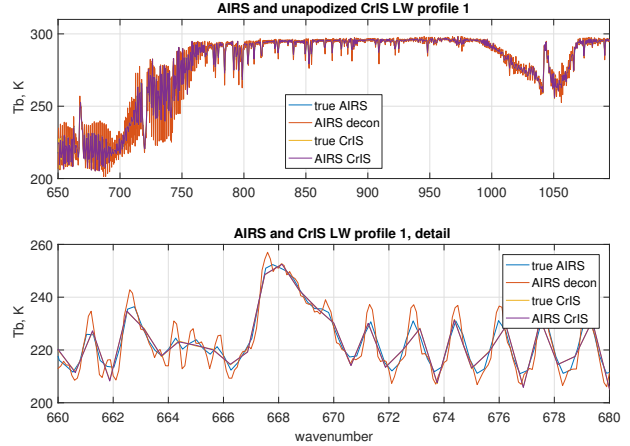


Figure 6: true AIRS, deconvolved AIRS, true CrIS, and AIRS CrIS. Differences between true CrIS and AIRS CrIS are too small to be visible in this figure.

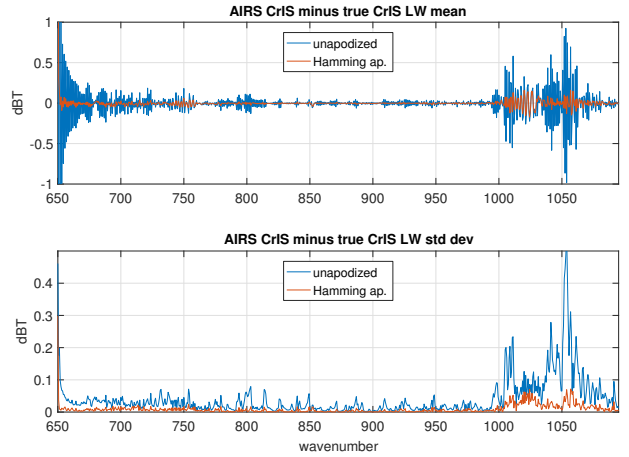


Figure 7: Mean and standard deviation of unapodized and Hamming apodized AIRS CrIS minus true CrIS, for the CrIS LW band

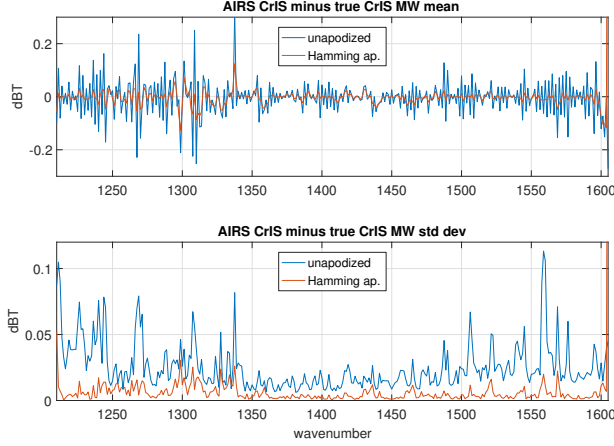


Figure 8: Mean and standard deviation of unapodized and Hamming apodized AIRS CrIS minus true CrIS, for the CrIS MW band

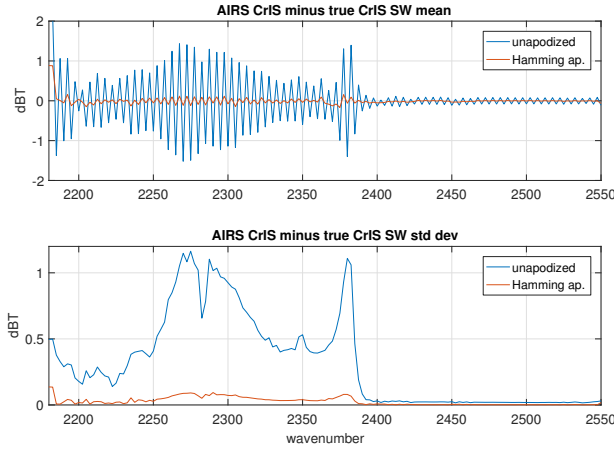


Figure 9: Mean and standard deviation of unapodized and Hamming apodized AIRS CrIS minus true CrIS, for the CrIS SW band

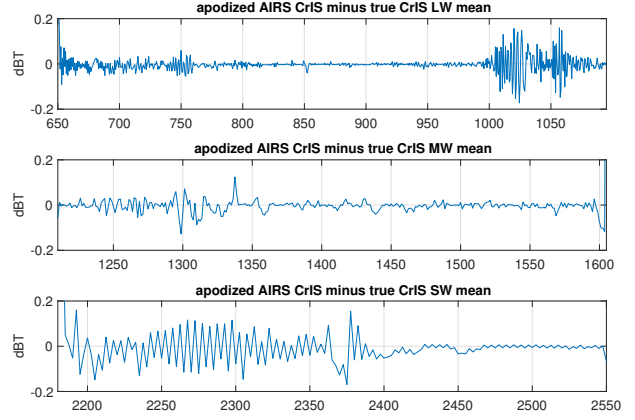


Figure 10: Mean of apodized residuals for all three CrIS bands

set. For the bias test we subtract the mean residual from the dependent set. For the linear test we find  $a_i$  and  $b_i$  to minimize  $\|a_i t_i^{\text{AC}} + b_i - t_i^{\text{TC}}\|_2$ , and for the quadratic test weights  $c_i$ ,  $a_i$  and  $b_i$  to minimize  $\|c_i (t_i^{\text{AC}})^2 + a_i t_i^{\text{AC}} + b_i - t_i^{\text{TC}}\|_2$ . The resulting correction is then applied to the independent set, the 49 fitting profiles, for comparison with true CrIS.

Figure 11 is a comparison of bias, linear, and quadratic corrections for the LW band. The linear and quadratic corrections are nearly identical, and the quadratic coefficient is very close to zero. Figure 12 shows the weights for the linear fits from figure 11. The  $a$  weights are very close to 1 and the  $b$  weight to the bias. Figures 13 and 14 show the linear correction giving a similar improvement in the MW and a small improvement in the SW, where the quadratic correction is noticeably worse. Figure 15 summarizes results for the linear correction, paired with the apodized uncorrected residuals.

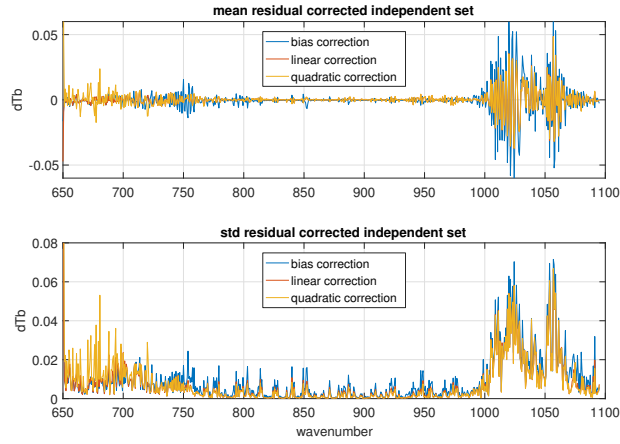


Figure 11: Mean and standard deviation of LW corrected apodized residuals

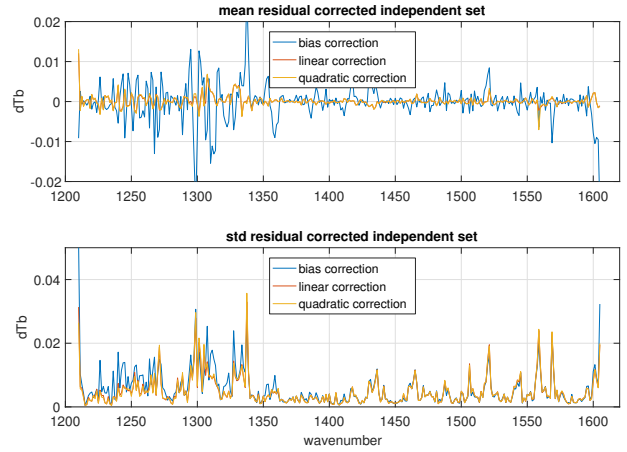


Figure 13: Mean and standard deviation of MW corrected apodized residuals.

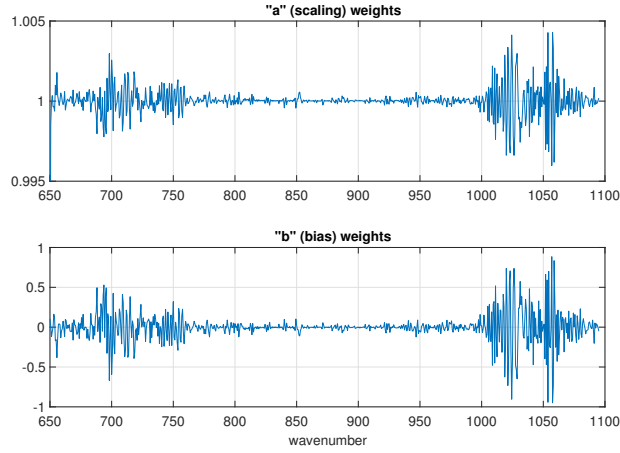


Figure 12: LW  $a$  and  $b$  weights for the linear correction  $ax + b$

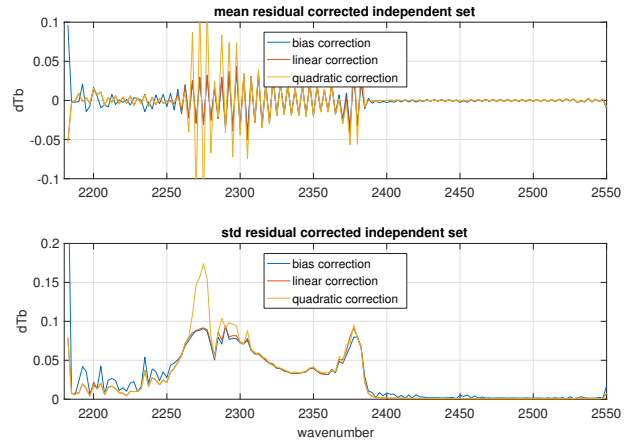


Figure 14: Mean and standard deviation of SW corrected apodized residuals.



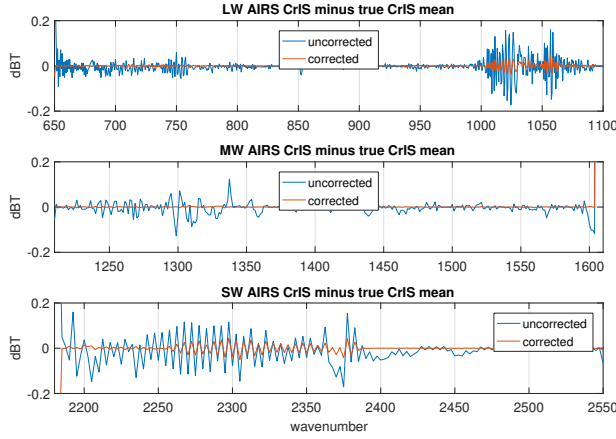


Figure 15: Mean corrected and uncorrected apodized residuals for all three bands.

We can give a good estimate of noise equivalent differential radiance (NEdN) for the translation by adding noise with a normal distribution at the AIRS NEdN to blackbody radiance at 280K and translating this to CrIS. This is done repeatedly and the noise after translation is measured. As a check, noise before translation is also measured and compared with the original AIRS value. The result, along with AIRS and CrIS NEdN, are shown in figure 16. The first subplot in figure 17 shows corresponding NEdT for fitting profile 1, for apodized CrIS and AIRS to CrIS radiances.

The AIRS and CrIS NEdN values are averages over a full day, 4 Dec 2016. NEdT for the L1c synthetic channels is interpolated. The AIRS channel-to-channel NEdN variation is significant; in the upper half of the LW and most of the MW it is the same order as the AIRS and CrIS NEdN difference. This variation is due the AIRS focal plane structure and sensitivity. Both AIRS and CrIS NEdN measures are spiky when averaged over a few minutes, but the CrIS variation is primarily uncertainty in the noise measurement, and smooths out as the time span is extended.

The AIRS to CrIS translation inherits this variability, which becomes a significant part of the difference between AIRS CrIS and true CrIS. For a common

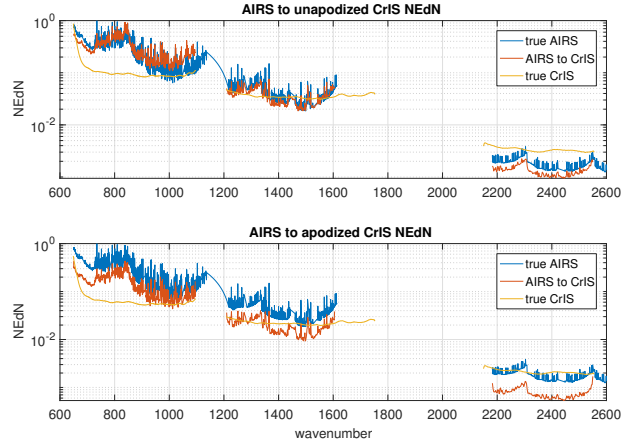


Figure 16: AIRS, AIRS-to-CrIS, and CrIS unapodized and apodized NEdN

record, we might want to add noise on a channel-by-channel basis to whichever NEdN value—AIRS CrIS or true CrIS—is lower. NEdN for the combined record would then be max of the AIRS CrIS and true CrIS NEdN values, as shown in the second subplot of figure 17.

The AIRS to CrIS translation via deconvolution works significantly better than conventional interpolation. We consider two cases. For the first, start with true AIRS and interpolate radiances directly to the CrIS user grid with a cubic spline. For the second, interpolate true AIRS to the  $0.1 \text{ cm}^{-1}$  intermediate grid with a cubic spline and then convolve this to the use CrIS user grid. Figure 18 shows interpolated CrIS minus true CrIS for the LW band, without apodization. The two-step interpolation works a little better than the simple spline, but both residuals are significantly larger than for the translation with deconvolution. Results for the MW are similar, while the unapodized comparison is less clear for the SW. With Hamming apodization, the residuals with deconvolution are significantly less than interpolation for all three bands.



## 4 Translation to an idealized grating model

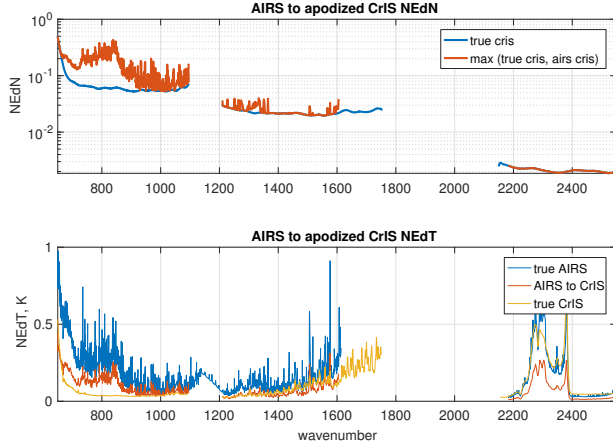


Figure 17: AIRS, AIRS-to-CrIS, and CrIS apodized NEdT, and the max of true CrIS and AIRS-to-CrIS NEdN, with true CrIS shown as a reference

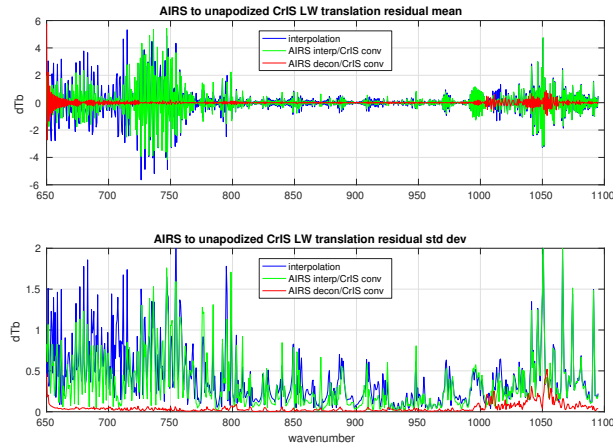


Figure 18: spline interpolation, interpolation with convolution, and deconvolution with convolution for the CrIS LW band

The AIRS deconvolution can be used for other translations. In this section we briefly consider reconvolution to an idealized grating model for resolving powers of 700 and 1200. Define an AIRS L1d basis with resolving power  $R$  from the generalized Gaussian response function of section 2 as follows. Let  $v_0$  be the frequency of the first channel and for  $i \geq 0$   $\text{FWHM}_i = v_i/R$ ,  $dv_i = \text{FWHM}_i/2$ , and  $v_{i+1} = v_i + dv_i$ . As with tests of the AIRS to CrIS translation, true L1c is calculated by convolving kcarta radiances with AIRS L1c SRFs and true L1d by convolving with an L1d basis at the desired resolving power. L1c is translated to L1d by deconvolution followed by reconvolution to the desired L1d basis, and this is compared with true L1d.

Figure 19 shows residuals for reconvolution to an L1d basis with resolving power of 1200, the nominal AIRS resolution, and figure 20 shows residuals for a resolving power of 700. Note the different x-axes for the two figures. The residuals depend in part on the L1d starting channel  $v_0$ , and so on how the L1c and L1d SRF peaks line up. The residuals shown are the result of a rough fit for  $v_0$ . For a resolving power of 1200 this gave  $v_0$  equal to the first L1c channel, while for 700 it was the first L1c channel plus  $0.2 \text{ cm}^{-1}$ .

We see that for both the AIRS to CrIS and L1c to L1d translations some resolving power is sacrificed in shifting channel centers to a single regular function of frequency. Residuals for a resolving power of 1200 (figure 19) are roughly comparable to unapodized CrIS (figures 7, 8, and 9) and residuals for a resolving power of 700 (figure 20) are roughly comparable to apodized CrIS (figure 15). As with the AIRS to CrIS translation, the L1c to L1d residuals are significantly reduced with a linear correction. Residuals for L1d with a resolving power of 700 after correction are comparable to residuals for apodized CrIS after a similar correction.

As with the AIRS to CrIS translation, deconvolution works significantly better than interpolation. We consider similar cases. For the first, start with true L1c and interpolate radiances directly to the L1d grid

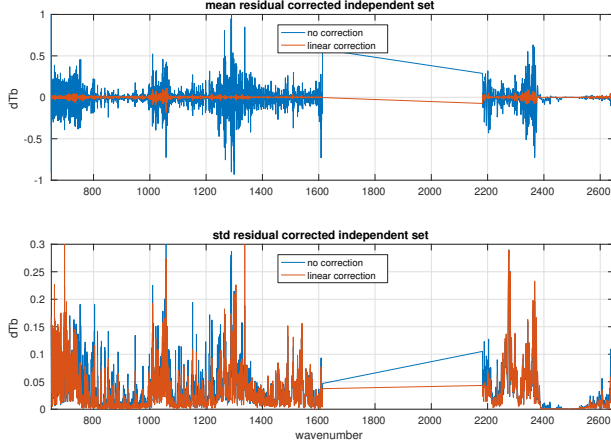


Figure 19: mean and standard deviation over the 49 fitting profiles for the L1c to L1d translation minus true L1d for a resolving power of 1200

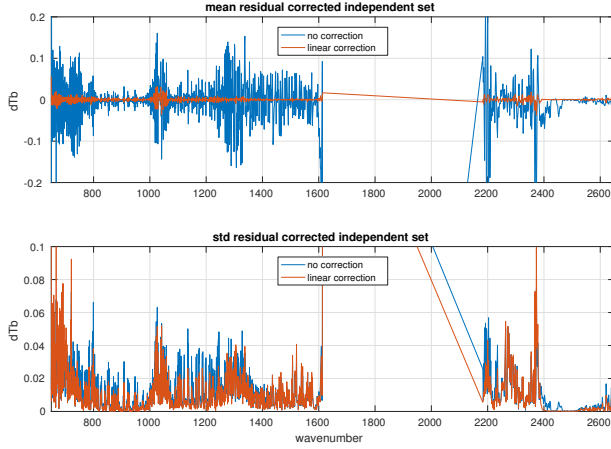


Figure 20: mean and standard deviation over the 49 fitting profiles for the L1c to L1d translation minus true L1d for a resolving power of 700

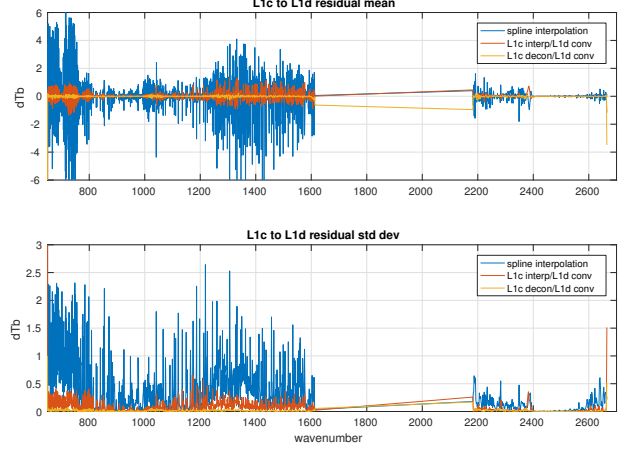


Figure 21: spline interpolation, interpolation with convolution, and deconvolution with convolution for the AIRS L1c to L1d translation with  $v_0 = 649.822 \text{ cm}^{-1}$  and a resolving power of 700

with a cubic spline. For the second, interpolate true L1c to the  $0.1 \text{ cm}^{-1}$  intermediate grid with a cubic spline and convolve this to the L1d channel set. Figure 21 shows interpolated L1d minus true L1d. The two-step interpolation works a little better than the simple spline, but is still much larger than the residual for translation with deconvolution.

## 5 Principal component regression

The AIRS L1c to L1d translation can be done with a single linear transform  $S_d \cdot S_c^{-1}$ , where  $S_c$  and  $S_d$  are the transforms taking the intermediate grid to L1c and L1d channels. The AIRS to CrIS translation can also be done with a composite transform if we use a resampling matrix rather than the double Fourier interpolation to go from the intermediate grid to the CrIS user grid. We can get such a one-step transform in other ways. For example if  $r_a$  and  $r_c$  are  $m \times k$  and  $n \times k$  AIRS and CrIS radiance sets, we can find  $X$  to minimize  $\|Xr_a - r_c\|_2$ . Typically  $k > m$ , giving an overdetermined system, and we solve  $r_a^t X^t = r_c^t$  for  $X$  by regression. This is different from the cor-

rections of section 3 and 4; there regression was used to find linear or quadratic correction coefficients independently for each channel.

Figures 22 and 23 show residuals for direct regression and deconvolution translation with statistical correction, both for apodized radiances. As before we use the 7377 profile set as the dependent and the 49 profile as the independent sets. The residuals are roughly comparable; the LW residual is larger at the low end of the band for direct regression and the high end for the deconvolved translation. Deconvolution does better in the MW, and direct regression in the SW.

Unfortunately the regression matrices show significant off-diagonal correlations. Figure 24 shows this for the LW; the MW and SW bands are worse. As noted in section 3 the 7377 profile dependent set is highly correlated. The effective dimension is only 260, our regression is actually under-determined. The dependent set residuals are close to zero, much less than the residuals for the independent set shown above.

One fix is to add noise. Recall that we generate true AIRS and true CrIS by convolving a common set of high-resolution radiances. For true AIRS we can simply add noise at the AIRS NEdN spec. But for regression or testing of an AIRS to CrIS translation we want CrIS radiances with actual translated AIRS noise, not simply true CrIS with noise added as per the CrIS NEdN spec. The latter does reduce correlations but increases residuals for the independent set significantly.

To model NEdN for the AIRS to CrIS translation we synthesize noise at the AIRS NEdN spec, add it to the signal, run it through the translation, and measure it. That works fine for measuring noise. But to get an AIRS to CrIS translation by regression with added noise we need the reference translation of each noisy AIRS spectra. One way to do that might be to add noise to the high res spectra before convolution to the AIRS user grid in such a way that we match the AIRS NEdN spec and convolve this noisy signal to the CrIS user grid to get noisy CrIS, but we do not pursue that further here.

As an alternative to adding noise, we can use a form of principal component regression. As above,

let  $r_a$  and  $r_c$  be  $m \times k$  and  $n \times k$  AIRS and CrIS radiance sets. Let  $r_a = U_a S_a V_a^T$  be the singular value decomposition with singular values in descending order and  $U_a^i$  the first  $i$  columns of  $U_a$ . Similarly let  $r_c = U_c S_c V_c^T$  be a singular value decomposition with singular values in descending order and  $U_c^j$  the first  $j$  columns of  $U_c$ . Let  $\hat{r}_a = (U_a^i)^T r_a$  and  $\hat{r}_c = (U_c^j)^T r_c$  be  $r_a$  and  $r_c$  represented with respect to the bases  $U_a^i$  and  $U_c^j$ . Since these are orthonormal, the transpose is the inverse. Then as before find  $X$  to minimize  $\|X\hat{r}_a - \hat{r}_c\|_2$  by solving  $\hat{r}_a^T X^T = \hat{r}_c^T$  for  $X$  by regression. This gives us  $R = U_c^j X (U_a^i)^T$ , an AIRS to CrIS transform parameterized by the AIRS and CrIS basis sizes  $i$  and  $j$ ,

Note that this sort of principal component regression is not the same as regression after principal component (or singular vector) filtering; for that we would take  $\bar{r}_a = U_a^i (U_a^i)^T r_a$ ,  $\bar{r}_c = U_c^j (U_c^j)^T r_c$ , find  $X$  to minimize  $\|X\bar{r}_a - \bar{r}_c\|_2$ , and have no need for a change of bases to apply  $X$ . In practice this did not work as well as doing regression after the change of bases.

Figure 25 shows residuals and figures 26, 27, and 28 the transform  $R$  for the CrIS LW, MW, and SW bands. We have chosen  $i = j = 500$  for the LW,  $i = 500$  and  $j = 320$  for the MW, and  $i = j = 100$  for the SW, to roughly balance unwanted correlation with residual size. For all three bands the residuals for principal component regression are larger than for the deconvolution translation with regression correction and there is still significant off-diagonal correlation, especially for the MW and SW bands. We conclude the deconvolution translation with regression correction works significantly better than regular or principal component regression, although the latter does work better than conventional interpolation.

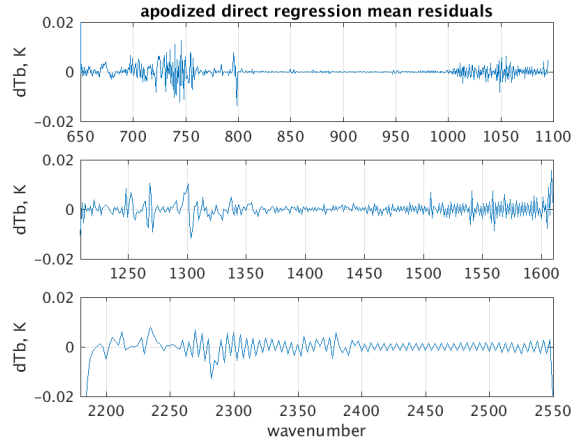


Figure 22: mean residuals for apodized AIRS to CrIS direct regression

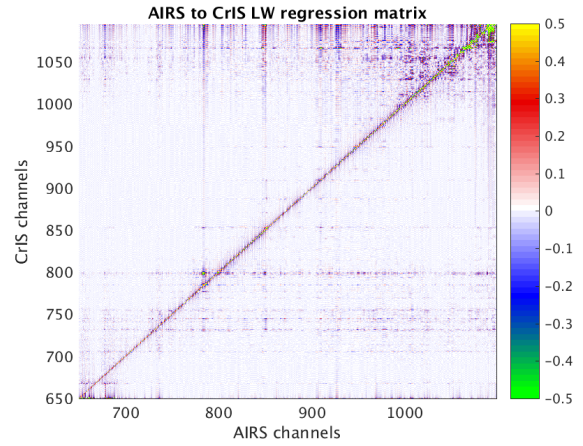


Figure 24: regression coefficients for the LW direct regression

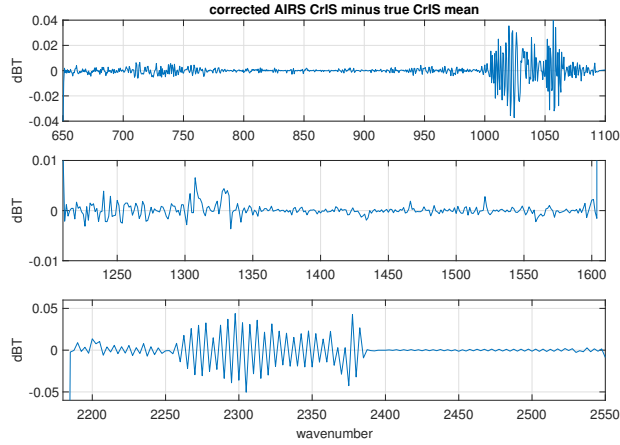


Figure 23: mean residuals for apodized AIRS to CrIS deconvolution translation with the regression correction

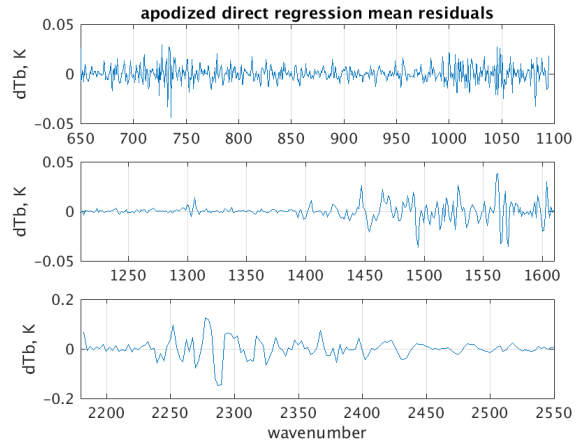


Figure 25: mean residuals for apodized AIRS to CrIS principal component regression

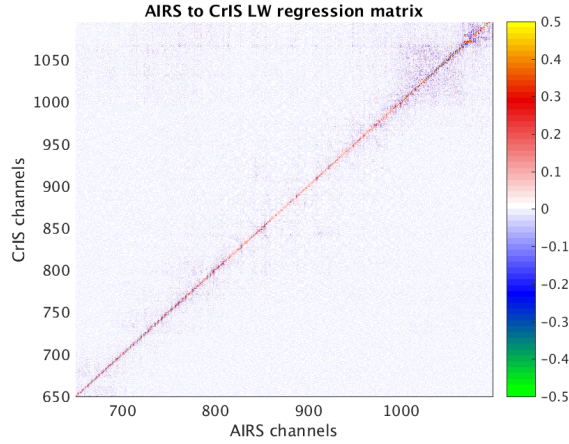


Figure 26: regression coefficients for the LW principal component regression

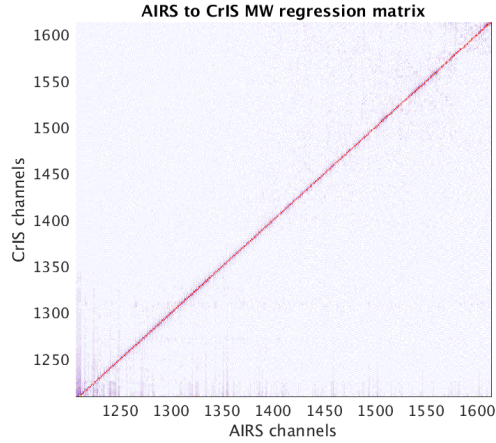


Figure 27: regression coefficients for the MW principal component regression

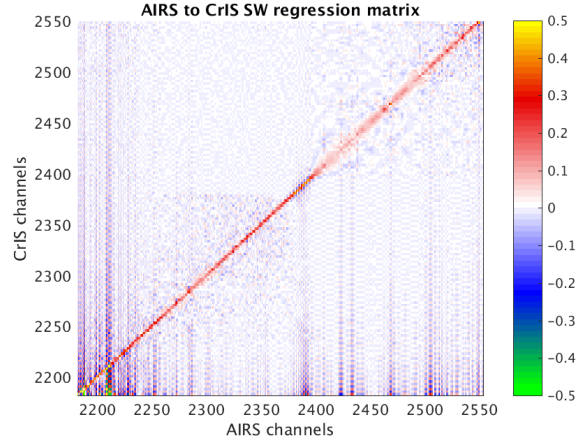


Figure 28: regression coefficients for the SW principal component regression

## 6 Conclusions

We have shown how to take advantage of detailed knowledge of the AIRS spectral response functions to deconvolve channel radiances to a resolution-enhanced intermediate representation, typically a  $0.1 \text{ cm}^{-1}$  grid. This deconvolution by itself gives a modest resolution enhancement at the cost of added artifacts and noise, but the main application is reconvolution to an alternate instrument specification. We consider two cases: reconvolution to the CrIS user grid, and to an idealized grating model. This translation works well by itself but can be improved with a linear correction applied independently to each channel, with coefficients determined by regression. Finally, we consider principal component regression directly from AIRS to CrIS radiances, and find a tradeoff between residual size and undesired correlations. Reducing the correlations increases the residuals, which become larger than for translation with deconvolution.

These ideas have been implemented and tested extensively, with Matlab demo code published on github. Our demos are i/o bound, but the in-core time for the AIRS to CrIS translation is divided into roughly 25 percent for the deconvolution and 75 percent for reconvolution, about 22 seconds to process

our 7377 profile cloudy test set on one compute node. Calculating the pseudo-inverse adds another 12 seconds, but that only needs to be done when the translation parameters change.

## 7 Appendix

We want to measure the correlation of a set of radiances. One such measure is dimension of a spanning set. For an approximation we use the basis size needed to get reconstruction residuals below some fixed threshold. Let  $r_0$  be an  $m \times n$  array of radiances, one row per channel and one column per observation. Let  $r_1 = USV^T$  be a singular value decomposition with singular values in descending order and  $U_k$  the first  $k$  columns of  $U$ . Let  $r_k = U_k U_k^T r_0$ ; then  $r_k \approx r_0$ . The approximation improves as  $k$  increases and becomes exact for some  $k \leq m$ . This is the analog of principal component filtering using left-singular rather than eigenvectors and is useful as a form of compression when  $k$  is small relative to  $n$ . For that case we save  $U_k$  and  $U_k^T r_0$  separately. Applications include compression of IASI radiance data and the karta absorption coefficient database.

We use a threshold for equivalence that is relevant for our applications. Let  $B^{-1}$  be the inverse Planck function and define  $d(r_1, r_2) = \text{RMS}(B^{-1}(r_1, v) - B^{-1}(r_2, v))$ , the RMS difference over all channels and observations of the brightness temperatures of radiance data. Finally let  $j$  be the smallest value such that  $d(r_0, r_j) \leq T_d$ , for some threshold  $T_d$ . Then  $j$  is the effective dimension of our set  $r_0$ . Here we have chosen  $T_d = 0.02$  K. For the 49 profile fitting set this gives  $j = 48$ , which we interpret as largely uncorrelated, while for the 7377 profile cloudy set we found  $j = 260$ , which we interpret as highly correlated.

## References

- [1] H. H. Aumann, M. T. Chahine, C. Gautier, M. D. Goldberg, E. Kalnay, L. M. McMillin, H. Revercomb, P. W. Rosenkranz, W. L. Smith, D. H. Staelin, L. L. Strow, and J. Susskind. AIRS/AMSU/HSB on the aqua mission: design, science objectives, data products, and processing systems. *IEEE Transactions on Geoscience and Remote Sensing*, 41:253–264, Feb. 2003.
- [2] Y. Han, H. Revercomb, M. Crompt, D. Gu, D. Johnson, D. Mooney, D. Scott, L. Strow, G. Bingham, L. Borg, Y. Chen, D. DeSlover, M. Esplin, D. Hagan, X. Jin, R. Knuteson, H. Motteler, J. Predina, L. Suwinski, J. Taylor, D. Tobin, D. Tremblay, C. Wang, L. Wang, L. Wang, and V. Zavyalov. Suomi NPP CrIS measurements, sensor data record algorithm, calibration and validation activities, and record data quality. *Journal of Geophysical Research (Atmospheres)*, 118(D17):12734, Nov. 2013.
- [3] C. Hepplewhite and L. L. Strow. A Hyper-Spectral Multi-Sensor Infrared Radiance Data Record for Climate Trending: Validation using Simultaneous Nadir Observations. in preparation, UMBC/JCET, 2017.
- [4] E. M. Manning, H. H. Aumann, D. A. Elliott, and L. L. Strow. AIRS Level 1C Algorithm Theoretical Basis. Version 3.0, Jet Propulsion Laboratory, Jan. 2015.
- [5] H. E. Motteler and L. L. Strow. Interferometric Interpolation. [https://github.com/strow/airs\\_deconv/blob/master/doc/finterp.pdf](https://github.com/strow/airs_deconv/blob/master/doc/finterp.pdf), 2014.
- [6] H. E. Motteler and L. L. Strow. Deconvolution and translation between high spectral resolution IR sounders. [https://github.com/strow/airs\\_deconv/blob/master/decon.pdf](https://github.com/strow/airs_deconv/blob/master/decon.pdf), 2016.
- [7] H. E. Motteler and L. L. Strow. AIRS and CrIS sampling comparisons. [https://github.com/motteler/cris\\_telecon/blob/master/airs\\_cris\\_obs/airs\\_cris.pdf](https://github.com/motteler/cris_telecon/blob/master/airs_cris_obs/airs_cris.pdf), 2017.
- [8] L. Strow, S. Hannon, S. De Souza-Machado, H. Motteler, and D. Tobin. An overview of the airs radiative transfer model. *Geoscience and Remote Sensing, IEEE Transactions on*, 41(2):303–313, Feb 2003.

- [9] L. L. Strow, S. E. Hannon, S. De-Souza Machado, H. E. Motteler, and D. C. Tobin. Validation of the atmospheric infrared sounder radiative transfer algorithm. *Journal of Geophysical Research: Atmospheres*, 111(D9), 2006. D09S06.
- [10] L. L. Strow, H. Motteler, D. Tobin, H. Revercomb, S. Hannon, H. Buijs, J. Predina, L. Suwinski, and R. Glumb. Spectral calibration and validation of the Cross-track Infrared Sounder on the Suomi NPP satellite. *Journal of Geophysical Research (Atmospheres)*, 118(D17):12486, Nov. 2013.
- [11] L. L. Strow, H. E. Motteler, R. G. Benson, S. E. Hannon, and S. D. Souza-Machado. Fast computation of monochromatic infrared atmospheric transmittances using compressed look-up tables. *Journal of Quantitative Spectroscopy and Radiative Transfer*, 59(35):481 – 493, 1998. Atmospheric Spectroscopy Applications 96.
- [12] Wikipedia contributors. Gaussian function, Wikipedia, the free encyclopedia. <http://en.wikipedia.org/w/index.php?title=Gaussian%20function&oldid=797726014>, 2017. [Online; accessed 10-September-2017].
- [13] Wikipedia contributors. Moore–Penrose pseudoinverse, Wikipedia, the free encyclopedia. <http://en.wikipedia.org/w/index.php?title=Moore%E2%80%93Penrose%20pseudoinverse&oldid=798542494>, 2017. [Online; accessed 10-September-2017].